Evanescent wave cavity ring-down spectroscopy with a total-internal-reflection minicavity

Andrew C. R. Pipino,[a] Jeffrey W. Hudgens, and Robert E. Huie
Physical and Chemical Properties Division, Chemical Science and Technology Laboratory, National Institute of Standards and Technology, Gaithersburg, Maryland 20899

(Received 13 December 1996; accepted for publication 15 May 1997)

A miniature-cavity realization of the cavity ring-down concept, which permits extension of the technique to spectroscopy of surfaces, thin films, liquids, and, potentially, solids, is explored using a wave-optics model. The novel spectrometer design incorporates a monolithic, total-internal-reflection-ring cavity of regular polygonal geometry with at least one convex facet to induce stability. Evanescent waves generated by total-internal reflection probe absorption by matter in the vicinity of the cavity. Optical radiation enters or exits the resonator by photon tunneling, which permits precise control of input and output coupling. The broadband nature of total-internal reflection circumvents the narrow bandwidth restriction imposed by dielectric mirrors in conventional gas-phase cavity ring-down spectroscopy. Following a general discussion of design criteria, calculations are presented for square and octagonal cavity geometries that quantify intrinsic losses and reveal an optimal cavity size for each geometry. Calculated absorption spectra for the NO_3 radical from 450 to 750 nm in a nitric acid solution are presented to demonstrate bandwidth and sensitivity. [S0034-6748(97)03808-2]

I. INTRODUCTION

Cavity ring-down spectroscopy[1–6] (CRDS) has been demonstrated as a technique for the measurement of optical absorption that excels in the low-absorbance regime where conventional methods have inadequate sensitivity. CRDS utilizes the mean lifetime of photons in a high-finesse optical cavity as the absorption-sensitive observable. Typically, the cavity is formed from a pair of nominally equivalent, narrow band, ultrahigh reflectivity dielectric mirrors, configured appropriately to form a stable optical resonator. A laser pulse is injected into the cavity through a cavity mirror to experience a mean lifetime given by,[5]

$$\tau(\omega)=\frac{t_r/2}{|\ln R(\omega)|+\Sigma_i\sigma_i(\omega)\int_0^L N_i(\xi)d\xi}, \tag{1}$$

where t_r is the photon round-trip transit time for a cavity of length L, σ_i, and N_i are the absorption cross section and number density of species i, respectively, and $|\ln R(\omega)|$ accounts for intrinsic cavity losses arising largely from the frequency-dependent mirror reflectivities when diffraction losses are negligible. The determination of optical absorption is, thereby, transformed from the conventional power-ratio measurement to a measurement of time. The ultimate sensitivity of CRDS is determined by the magnitude of the intrinsic cavity losses, which can be minimized with techniques such as superpolishing[7] that permit the fabrication of ultra-low-loss optics. Although CRDS has provided a rich variety of gas-phase spectroscopic[8–13] and kinetic[14–18] information, the method has not yet been extended to spectroscopy of the condensed state.[19] Extension of CRDS to condensed matter requires an innovative cavity design that circumvents the narrow bandwidth restriction of conventional CRDS, dielectric mirrors, while providing a low intrinsic cavity loss and a well-defined relationship between photon decay time and absorption.

In the following, a novel implementation of the cavity ring-down concept is investigated that utilizes the unique properties of total-internal reflection (TIR) to achieve a miniature-cavity realization of CRDS, which is applicable to condensed phase spectroscopy. Recently, small high-finesse cavities have attracted considerable attention in connection with microlasers,[20,21] harmonic conversion devices,[22,23] lasing,[24] fluorescence,[25] and spontaneous emission[26] in microdroplets, as well as a variety of other optical phenomena.[27–31] In many cases, high finesse is achieved by sustaining the cavity modes within a monolithic TIR ring, which eliminates Fresnel reflections associated with intracavity interfaces and facilitates miniaturization. The efficiency of TIR is diminished from unity only by surface scattering when nonspecular loss mechanisms[32] can be neglected. Another natural consequence of TIR is the generation of evanescent waves, which are required to satisfy the boundary conditions on Maxwell's equations for light incident from a denser medium at an angle that exceeds the critical angle. The utility of evanescent waves in spectroscopy, especially for surface, thin-film and liquid-phase spectroscopic studies, is well established.[33] In the low-absorption limit, the energy loss per reflection due to absorption by matter located within the decay length of the evanescent wave, is linear in the number density.[34] The presence of evanescent waves also permits the precise control of resonator input and output coupling through photon tunneling,[22,23,35] which is commonly termed frustrated total reflection (FTR). Furthermore, the broadband nature of TIR supplants the bandwidth restriction that is characteristic of the multilayer, dielectric mirrors of conventional CRDS, thereby permitting broad spectral regions to be probed with a single device.

In this investigation, design criteria for a CRD spectrom-

[a]National Research Council postdoctoral associate/NIST; electronic mail: andrew.pipino@nist.gov

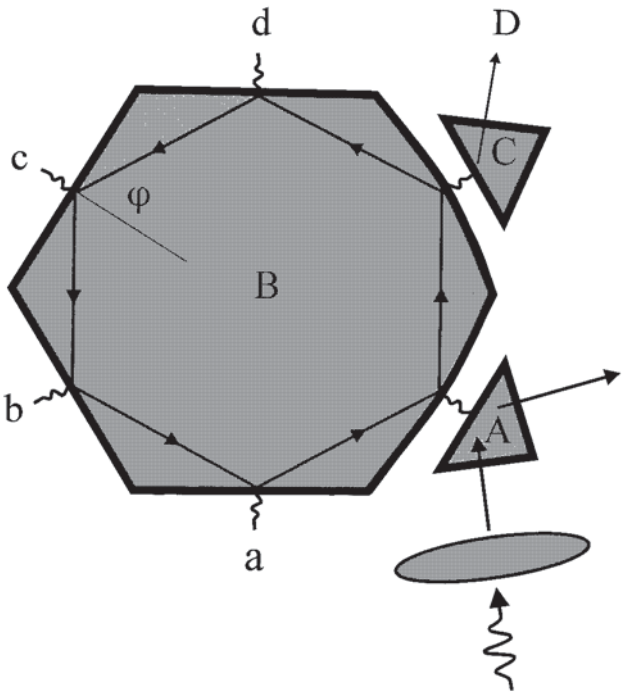

FIG. 1. A polygonal, TIR-ring resonator enables extension of the cavity ring-down concept to condensed matter spectroscopy. A light pulse is totally reflected by prism A, creating an evanescent wave, which excites the stable modes of the resonator B through photon tunneling. The absorption spectrum of matter located at the totally reflecting surfaces (a)–(d) is obtained from the mean lifetime of a photon in the monolithic cavity, which is extracted from the time dependence of the signal detected at D by out coupling with prism C.

eter that utilizes a monolithic TIR-ring cavity, as depicted in Fig. 1 for a hexagonal cavity, are elucidated and supported by a wave-optics model. Since each cavity design requires a custom optical fabrication, a theoretical analysis is appropriate to examine sources of intrinsic loss and the competition between intrinsic losses, which is somewhat unique to the TIR-ring cavity. In this initial investigation, the calculations are focused primarily on designs that can be realized by common optical fabrication methods, although alternative strategies, such as molecular beam epitaxy may be feasible.[21] Square and octagonal cavity geometries are considered, which permit thin films and bulk liquids to be probed in the visible, respectively, as discussed below. Schiller *et al.*[35] have characterized a square, fused-silica TIR-ring cavity under cw excitation conditions, which possessed a moderate finesse of ~5100. As these authors pointed out, the fabrication of a much higher finesse cavity should be feasible by selecting a higher grade of material and superpolishing the facets. The octagonal resonator offers a greater fabrication challenge, but should be feasible with existing technology. The combination of evanescent wave absorption with CRDS detection has recently been achieved in our laboratory through the use of a superpolished, fused-silica Pellin–Broca prism in a conventional CRDS cavity.[36] Despite moderately large polarization-dependent losses for this narrow-bandwidth cavity, submonolayer detection of I_2 at 625 nm was achieved. These results, together with theoretical predictions discussed below suggest that the TIR-ring cavity implementation of CRDS will provide a powerful new spectroscopic tool, which is especially well suited to surface and thin-film diagnostics. This paper contains three sections: (I) a general discussion of the relevant features of a polygonal TIR-ring resonator for CRDS, (II) a brief description of the theoretical model, and (III) quantitative results including intrinsic losses, determination of the optimal cavity size, and a calculated spectrum to demonstrate bandwidth and sensitivity.

II. GENERAL CONSIDERATIONS

A. Photon decay time

Zalicki and Zare[2] have shown that the minimum detectable absorbance change in conventional CRDS can be expressed as the product of the intrinsic cavity loss and the minimum detectable relative change in the photon decay time. For a monolithic, TIR-ring resonator, the cavity design that will yield maximum sensitivity arises from an interplay between the factors that optimize a conventional CRDS experiment and the factors that influence the magnitude of evanescent wave absorption. However, the round-trip time for a monolithic cavity is linked to bulk attenuation through the round-trip path length. Therefore, the resonator design that minimizes intrinsic loss, while providing a sufficiently long decay time to achieve maximum digitization accuracy, will be optimal for a given absorption loss.

In addition to bulk attenuation, other sources of loss, which can potentially reduce the mean photon lifetime, include surface scattering, diffraction, input and output coupling, and nonspecular effects. By analogy with Eq. (1), the photon decay time in a monolithic, TIR-ring cavity with n facets is given by

$$\tau(\omega)=\frac{t_r}{\mathscr{L}_{\text{bulk}}+\mathscr{L}_{\text{surf}}+\mathscr{L}_{\text{diff}}+\mathscr{L}_{\text{FTR}}+\mathscr{L}_{\text{nspec}}+(n-2)\Sigma_i\sigma_i(\omega)\int_0^{d_e}N_i(\xi)d\xi}, \tag{2}$$

where the total intrinsic cavity loss has been approximated by the sum of the individual round-trip losses, $\mathscr{L}_i$, and d_e is the effective sampling depth for the evanescent wave. In Eq. (2), two TIR surfaces are assumed to serve as coupling ports while the remaining n-2 surfaces sample the surrounding medium. For an n-sided ring resonator of refractive index n_i, the round-trip time is simply

$$t_r=n_iL_{\text{rt}}/c=2n(n_i/c)r_0\ \sin(\pi/n), \tag{3}$$

where r_0 is the inscribed-circle radius of the associated polygon and L_{rt} is the round-trip physical path length, which approaches $2\pi r_0$ in the limit as $n\to\infty$. The dependence of the photon decay time on the size of the cavity is incorporated directly in t_r and $\mathscr{L}_{\text{bulk}}$, while $\mathscr{L}_{\text{diff}}$ depends on cavity

size through the stability factors and the presence of apertures associated with the finite facet dimensions. For a resonator that is fabricated from a highly transparent material, the loss per pass due to bulk attenuation is approximated well by

$$\mathscr{L}_{\text{bulk}} = 2\alpha r_0 n \sin(\pi/n), \tag{4}$$

where α is the bulk attenuation coefficient. Note that as the size of the resonator is increased, such that bulk attenuation dominates, the photon decay time asymptotically approaches a constant value. An increase in cavity size beyond the point at which a sufficiently long decay time is obtained for accurate digitization, will only increase the minimum detectable absorbance change (decrease sensitivity). Clearly, an increase in cavity medium transmission will permit a lower detection limit to be achieved. In the visible and near-IR, fiber-optic-grade fused-silica and certain borosilicate glasses have an attenuation of 20 dB/km (46 ppm cm^{-1}) or less.[37] Several other materials have the potential to provide extremely high transmission in other spectral regions with the residual attenuation typically limited by multiphonon processes, defects, impurities, and phonon-assisted electronic transitions.[38]

When bulk attenuation is sufficiently small ($\sim$500 ppm/pass), surface scattering losses can become significant. Using scalar diffraction theory, the reduction in the mean specularly reflected intensity per round trip can be estimated from[39–41]

$$\mathscr{L}_{\text{surf}} \approx \left(\frac{4\pi n_i \sigma_{\text{RMS}} \sqrt{n} \cos\theta_i}{\lambda_0}\right)^2 = \left(\frac{4\pi n_i \sigma_{\text{RMS}} \sqrt{n} \sin(\pi/n)}{\lambda_0}\right)^2, \tag{5}$$

where σ_{RMS} is the root-mean-square surface roughness, λ_0 is the vacuum wavelength, and the angle of incidence, $\theta_i = \pi(n-2)/2n$, has been generalized for an n-sided polygonal resonator. Current optical polishing techniques and surface metrology allow ultrasmooth surfaces with $\sigma_{\text{RMS}} \sim 0.05$ nm to be fabricated routinely.[7] According to Eq. (5), scattering losses are thereby reduced to below 5 ppm per round trip at 600 nm for a square, fused-silica resonator with $\theta_i = 45°$. The strong incident-angle dependence in Eq. (5) also results in a reduction of the round-trip surface scattering loss for resonators with larger values of n, corresponding to larger angles of incidence, despite the increased number of total reflections. However, as will be shown, the reduction in surface scattering loss with increasing angle of incidence is counteracted by an increase in diffraction losses arising from apertures.

B. Resonator stability

The stability of ring resonators has been investigated previously.[42–45] By definition, a stable resonator supports one or more low-diffraction-loss modes, which are self-reproducing after one round-trip pass through the resonator.[46,47] Within the paraxial approximation, the stability conditions for an arbitrary n-element resonator can be obtained by first multiplying in sequence the ABCD matrices, M_i, associated with each element of the resonator to obtain the overall matrix for one round trip,[48] or

$$M_{\text{rt}} = M_1 M_2 M_3 \cdots M_n = \begin{pmatrix} A & B \\ C & D \end{pmatrix}. \tag{6}$$

From the self-consistency requirement, the condition for stability of the resonator is obtained as a constraint on the trace of the round-trip matrix, given by

$$\left|\frac{A+D}{2}\right| \leqslant 1. \tag{7}$$

For many-element resonators, the stability condition can become a complicated function of system parameters, but in general it can be expressed in terms of nondimensional ratios of radii of curvature to relevant separations. As in the case of a plane–parallel, linear resonator, a polygonal ring resonator consisting of n plane–parallel mirrors, satisfies the upper limit of Eq. (7), resulting in borderline instability with concomitant large diffraction losses since no refocusing occurs. However, the presence of a single convex facet induces stability, thereby substantially diminishing diffraction losses, as demonstrated by Schiller *et al.*[35] for a monolithic cavity. If the convex facet has a spherical radius, the effective focal lengths in the tangential and sagittal planes are then different, resulting in astigmatism. Two stability conditions must then be specified by the pair (X,Y), where $|X| \leqslant 1$ and $|Y| \leqslant 1$, in accordance with Eq. (7) for the tangential and sagittal planes, respectively.

C. Frequency selectivity

The transverse field distribution in a stable, astigmatic resonator is described to high accuracy by a modal decomposition in terms of the Hermite–Gauss functions.[48] A single transverse mode can be expressed as a product of two Hermite–Gauss functions that possess different orders and waist sizes in the tangential and sagittal planes. For a given system aperture size, diffraction losses are generally larger for higher-order transverse modes. The role of cavity transverse and longitudinal mode structure in CRDS has been discussed.[2,3,4,49] The effect can be significant, since the discrete mode spectrum can result in loss of spectral information if an absorption line is located between mode frequencies or can cause inefficient coupling if the bandwidth of the pulsed excitation source is narrow compared to the mode spacing. The polarization-dependent mode frequencies $\omega_{q,m,k}$ for an n-sided monolithic, TIR-ring cavity are given by[22]

$$\omega_{q,m,k}^{s,p} = \frac{c}{n_i L_{\text{rt}}}\left[2\pi q + \phi_x^k + \phi_y^m - \sum_{j=1}^{n} \gamma_{s,p}^{(j)}\right], \tag{8}$$

where ϕ_x and ϕ_y are the transverse mode-dependent Guoy phase shifts,[48] and the $\gamma^{(j)}$ are the polarization-dependent TIR phase shifts.[35] Although the broad absorption lines typi-

cally associated with condensed matter spectroscopy reduce the chances that spectral information will be lost, the large free-spectral range implied by Eq. (8) for small cavities could result in inefficient coupling if ~10 ns pulse width excitation sources, which are common in CRDS, are applied in a minicavity experiment. The ideal temporal width will be 0.1–1 ns, based on an optimized cavity size (*vide infra*), which maintains the ratio of the source linewidth to the longitudinal mode spacing.[4]

To circumvent the complications associated with a large free-spectral range, Meijer *et al.*[50] used a nondegenerate cavity with intentional mode mismatching to excite a quasicontinuum of transverse modes within the longitudinal mode free-spectral range of a conventional linear cavity. Mode mismatching may be an important strategy in minicavity CRDS to assure efficient coupling when relatively narrowband sources are used. This strategy determines the minimum useful cavity size, since the excited high-order modes must experience essentially the same photon decay time as the fundamental mode. Therefore, the resonator apertures must be large enough to render diffraction losses negligible for the highest-order mode with significant intensity. As the number of facets is increased, the facet size is decreased for a given L_{rt}, thereby further restricting the minimum useful cavity size. Alternatively, mode matching could have benefits such as providing a well-characterized probe field or a narrow bandwidth for high-resolution spectroscopy[3] in addition to a reduced diffraction loss for a given cavity size. Efficient mode matching to the lowest-order astigmatic modes of square and trigonal ring resonators has been achieved.[22] In comparison to linear resonators of conventional CRDS, the inherent mechanical stability of monolithic devices simplifies precise mode matching, since the resonance frequency can be scanned thermally or electro-optically.

D. Input–output coupling

In contrast to linear resonators of conventional CRDS, direct coupling of a free-space wave to the stable modes of a monolithic resonator cannot generally be achieved when the modes are sustained entirely by TIR. Spherical resonators, which support high-Q whispering gallery modes,[51] provide an exception. However, these non-Gaussian modes are difficult to mode match selectively.[31,41] CRDS requires the excitation of a consistent set of transverse modes to provide consistent sampling of an absorption spectrum. As shown schematically in Fig. 1, the modes of a TIR-ring resonator can be excited by photon tunneling[22] when totally reflecting prisms are placed in close proximity to the resonator such that the evanescent field is phase matched to the resonator modes. Although the presence of any radiative channel inherently degrades finesse, a key advantage of using photon tunneling for input and output coupling is the ability to control the extent of coupling through precise positioning of the coupling element with respect to the resonator. The use of separate facets for input and output eliminates the need for temporal separation of the high-energy reflected input pulse from the weak photon decay signal.

As discussed by Schiller *et al.*,[35] TIR-ring cavity transmission involves two tunneling processes that are resonance enhanced, thereby resulting in a gap-width-dependent coupling, finesse, and resonance frequency. Depending on the cavity geometry, the indices of refraction, the wavelength, and the total round-trip loss, a gap width will exist for which the coupling loss equals the total round-trip intrinsic loss of the resonator leading to impedance-matched coupling. For smaller gap widths, over coupling results with a concomitant degradation of finesse, while for larger gap widths, coupling efficiency plateaus as the uncoupled finesse limit is approached. Under impedance-matched conditions, the coupling efficiency is unity on resonance and the finesse is equal to one-half its maximum value. In applying a TIR-ring cavity for CRDS, operation in the weak-coupling regime is preferred to obtain maximum finesse. Although light throughput is reduced in this limit, signal levels can be enhanced through multiple mode excitation or mode-matched cw excitation.[52–54] Typically, in CRDS measurements, high signal-to-noise ratios are obtained, even when extremely high-finesse cavities and single mode excitation are employed.[55]

E. Nonspecular effects

In addition to bulk attenuation, surface scattering, diffractive, and coupling losses, a transmission loss can result from nonspecular reflection,[32] which arises when a finite diameter beam undergoes total reflection in the vicinity of the critical angle. An intuitive interpretation of nonspecular phenomena is obtained by considering the beam in terms of its angular spectrum of plane waves.[56] A finite beam diameter implies a distribution of wave vectors in the angular spectrum, with an inverse proportionality between beam diameter and spectral width. Since the Fresnel reflection coefficients are derived strictly for an infinite plane wave, the reflection of a finite beam cannot be expressed by a single Fresnel reflection coefficient. Instead, each component in the angular spectrum experiences a different phase and amplitude modification, resulting in nonspecular phenomena. A variety of aberrations arise from nonspecular reflection, including the well-known Goos–Hanchen lateral beam shift,[57] in which the apparent surface of geometric reflection is displaced normally to the interface. In a photon tunneling geometry, the Goos–Hanchen shift has been shown to occur equally for the reflected and transmitted beams.[58] The specific case of nonspecular reflection of Gaussian beams has been examined in detail[59] with a recent three-dimensional treatment proposing a complete description based on 20 independent effects.[60]

For a TIR-ring cavity implementation of CRDS, the potential for introduction of an additional intrinsic cavity loss is worth examining. Schiller[41] calculated the transmission loss exactly for a Gaussian beam incident near the critical angle for a fused silica/vacuum interface. The loss was well approximated by the expansion,

$$T=\frac{\exp(-\xi^2)}{-2\xi\sqrt{\pi}}\left(1-\frac{1}{2\xi^2}+\cdots\right), \tag{9}$$

where $\xi=(2\pi n_i/\lambda_0)\omega_x \sin(\theta_c-\theta_i)/\sqrt{2}$. For an angle of incidence that exceeds the critical angle, θ_c, by at least 1°, a loss of below 1 ppm is found for a beam waist of $\omega_x \sim 20\ \mu$m at 600 nm, suggesting that nonspecular transmission loss will be small relative to other sources of loss.

F. Evanescent wave absorption

The extent of evanescent wave absorption by a film of given thickness and absorptivity is a function of the angle of incidence and the index discontinuity at the totally reflecting surface, which determine the amplitude and penetration depth of the evanescent field.[33] In attenuated total reflectance (ATR) spectroscopy, this dependence is incorporated in the effective sampling depth,[34] which corresponds to the equivalent thickness required to obtain the same spectral contrast from a transmission experiment. As the angle of incidence approaches the critical angle or as the index discontinuity is reduced, the effective sampling depth increases, thereby augmenting sensitivity through an increase in path length as well as an enhancement of the local electric field. Although a general solution for TIR from stratified media can be found,[61] simple expressions for the effective sampling depth can be obtained immediately in the weak absorption limit for bulk materials or films that are thin relative to the evanescent wave decay length. For a thin film, direct comparison to a transmission spectrum is possible. For bulk materials, a linear dependence of the effective sampling depth on wavelength results in band distortion due to enhanced sensitivity at longer wavelengths. The effective sampling depth provides an established and simple relationship between the absorption loss per pass in a resonator and the mean photon lifetime as well as a well-defined path length for quantitative spectroscopy.

For TIR-ring resonators, stable modes are sustained when the angle of incidence for the chief ray (or beam center), given by $\theta_i=\pi(n-2)/2n$, exceeds the critical angle, $\vartheta_c=\sin^{-1}(n_0/n_i)$. Therefore, a discrete set of allowed angles of incidence exists for a given index discontinuity. The incident angle that is closest to the critical angle will provide maximum sensitivity and the smallest value of n. Since TIR is not frustrated by films that are thin relative to the evanescent wave decay length regardless of the film refractive index, the simplest resonator design that supports stable modes in vacuum can be used for thin-film diagnostics. For bulk materials, the optimum resonator geometry will depend on the index discontinuity. The value of n must be selected to prevent frustrating the total reflection or incurring losses due to nonspecular effects as θ_i approaches θ_c. When n is increased to compensate for a decreasing index discontinuity, detection sensitivity is enhanced due to the larger number of total reflections, although the resulting resonator may present a greater fabrication challenge.

III. THEORETICAL MODEL

To quantitatively evaluate performance and to search for an optimum resonator design, a general polygonal-ring-resonator model was developed. Since diffraction losses account for a significant fraction of the total system loss as the resonator size is decreased to reduce bulk attenuation, a wave-optics formalism within the scalar Fresnel approximation was employed. A global coordinate system was used to specify the beam front and TIR facet positions. Beam transverse profiles were represented by two 512×512 complex arrays, corresponding to the orthogonal polarization components. Photon tunneling was integrated into the model by following the development of Court and Von Willisen,[62] which excludes nonspecular effects. Beam propagation was computed by applying Fourier transform methods to Huygens' integral, as discussed below. Calculations were implemented using the General Laser Analysis and Design code (Applied Optics Research, Pittsford, N.Y.) on a Cray 90.[63] Several subtleties associated with the use of scalar Fresnel theory for quantitative evaluation of diffraction effects in optical resonators are discussed below.

Huygens' integral expresses the intuitive notion that a wave front at one position along the optic axis can be constructed from knowledge of the wave front at a different position by treating each point on the initial wave front as a spherical wave source. For propagation along the z axis from the plane $z=z_1$, Huygens' integral is given by

$$E(x_2,y_2,z_2)=i\frac{n_i}{\lambda_0}\int\int_{S_1}E(x_1,y_1,z_1)\times\frac{\exp}{|\mathbf{r}|}\left(i\frac{-2\pi n_i}{\lambda_0}|\mathbf{r}|\right)\cos\theta\,dx_1dy_1, \quad (10)$$

where $S_1(x_1,y_1,z_1)$ corresponds to the initial wave-front surface and θ is the angle between the normal to the wave front at a source point and the vector $\mathbf{r}=(x_2-x_1)\mathbf{i}+(y_2-y_1)\mathbf{j}+(z_2-z_1)\mathbf{k}$, which connects the source point to a point on the final wave front. By expanding the radical expression arising from $|\mathbf{r}|$ to second order in the exponent and first order in the denominator and setting the $\cos\theta=1$, Huygens' integral within the Fresnel approximation is obtained, which is given by

$$E(x_2,y_2,z_2)\sim\frac{in_i\exp[-2\pi in_i(z_2-z_1)/\lambda_0]}{\lambda_0(z_2-z_1)}\times\int\int_{S_1}E(x_1,y_1,z_1)\times\exp\left[i\frac{-\pi n_i}{\lambda_0}\frac{(x_2-x_1)^2+(y_2-y_1)^2}{(z_2-z_1)}\right]\times dx_1\,dy_1. \quad (11)$$

Using the convolution theorem, Eq. (11) can be computed according to[48,56]

$$E(x_2,y_2,z_2)=\frac{\exp[i\pi n_i|\mathbf{r}_2|^2/\lambda(z_2-z_1)]}{i\lambda(z_2-z_1)}\times\mathscr{F}\left[E(x_1,y_1,z_1)\exp\left(i\frac{\pi n_i|\mathbf{r}_1|^2}{\lambda(z_2-z_1)}\right)\right], \quad (12)$$

where $|r_i|^2 = x_i^2 + y_i^2 + z_i^2$ and $\mathcal{F}[\ ]$ implies Fourier transformation. This approach to computing propagation is equivalent to the more intuitive angular spectrum decomposition method. As discussed in standard texts,[48,56] the angular spectrum method proceeds by Fourier transformation of the field distribution, propagation of the resulting plane-wave components, followed by inverse transformation, according to

$$E(x_2,y_2,z_2) = \mathcal{F}^{-1}[\exp(-i\lambda_0 k_0^2 (z_2 - z_1)/4\pi n_i) \times \mathcal{F}[E(x_1,y_1,z_1)]], \tag{13}$$

with $k_0^2 = k_x^2 + k_y^2$, where the k_i correspond to spatial frequencies in the x and y directions, which are associated with a particular plane-wave component. However, in the discrete domain the quadratic phase factors in Eqs. (12) and (13) can give rise to aliasing errors if the same algorithm is used for computing both near- and far-field propagation. Therefore, Eq. (12) is used for far-field propagation since the quadratic phase factor varies slowly as $z - z_0 \to \infty$ and rapidly as $z - z_0 \to 0$, while Eq. (13) is used for near-field propagation. Consistent selection of the beam propagation algorithm is especially important in modeling resonators, since the self-consistency condition will not be satisfied if the algorithms are applied inconsistently over a round trip for a system with internal foci. To guarantee consistent algorithm selection, a ''surrogate'' Gaussian beam is used,[63] which is the best-fit Gaussian beam to the distribution. The surrogate Gaussian beam serves only in algorithm selection, which is based on the position of the actual beam front relative to the waist of the surrogate beam. When the injected beam is within the Rayleigh range of the surrogate beam, the near-field propagation algorithm [Eq. (13)] is used with no rescaling of the grid. For propagation steps outside the Rayleigh range, the far-field algorithm [Eq. (12)] is employed and the distribution is rescaled to account for diffraction-induced spreading. Use of the surrogate Gaussian beam for propagation control allows an arbitrary distribution to be injected into the resonator to excite many transverse modes.

Diffraction losses arising from the sifting of modes by the system apertures are treated approximately by assuming rectangular apertures with dimensions determined by the facet projections in the direction orthogonal to the beam. In the plane of the resonator, an aperture width is determined by the number of facets n and L_{rt}. In the orthogonal direction, there is no inherent restriction so this dimension is assigned a sufficiently large value to eliminate any significant contribution to the diffraction loss. A rigorous solution to the problem of diffraction by a tilted aperture would account for the variable point-spread function across the aperture plane. However, the error introduced by neglecting the inhomogeneity of the system will be manifested only at high spatial frequencies, which can be understood intuitively by replacing the propagation distance $\Delta z = z_2 - z_1$ in Eqs. (12) or (13) with z_{eff} an ''effective'' propagation distance, which provides the correct solution. Since $z_{\mathrm{eff}} \sim \Delta z$, the beam profile after a propagation of a distance Δz will differ from a beam propagated a distance z_{eff} only at high spatial frequencies.[48,63]

Since the aperture size is associated with the facet dimensions, the propagation distance between facets is a few times the in-plane aperture width for regular, polygonal resonators. In this close proximity to the aperture, scalar Fresnel theory begins to break down for high spatial frequencies,[48] so that the approximate treatment of the tilted aperture maintains the level of approximation of the scalar Fresnel theory. Feiock[64] investigated the accuracy of the Fresnel approximation for diffraction by a uniformly irradiated rectangular aperture when the propagation distance beyond the aperture was comparable to the aperture width (high Fresnel numbers). The on-axis amplitude was found to be accurately determined, while the amplitude near the aperture edge differed by a few percent from the value calculated using the next level of approximation to Huygens' integral, which improves the accuracy at higher spatial frequencies. To test the sensitivity of our calculated results to high spatial frequencies, calculations with increasing grid density were examined, yet only small changes, typically, less than a few percent, were observed in the energy loss. These results suggest that scalar diffraction theory within the Fresnel approximation provides a sufficiently accurate assessment of diffraction losses for the problem of interest.

IV. RESULTS AND DISCUSSION

To demonstrate the essential characteristics of monolithic TIR-ring resonators that are relevant to CRDS, numerical results for cavities based on square and octagonal geometries are presented. The cavity material is assumed to be fiber-optic-grade fused silica ($n = 1.458$, -10 dB/km at 633 nm) for all calculations, except where noted. The square resonator was investigated since the nominal angle of incidence of 45° is close to the critical angle of 43.3°, providing maximum sensitivity. In addition, the nominally square cavity is the simplest possible fused-silica stable resonator and can be considered as the basic building block for a device analogous to the rectangular waveguide. The relatively low index of refraction for fused silica requires that the square resonator be applied as a thin-film probe, since, in accordance with the critical angle condition, the total reflection will be frustrated by most thick films or liquids. To investigate an appropriate design for application to dilute aqueous solutions, the fused-silica octagonal resonator was considered. The use of higher-index cavity materials, such as ultra-high-purity glasses, permits higher-index solutions to be examined. This is demonstrated in a spectral simulation in which an ultra-high-purity-glass octagonal resonator is utilized to probe a nitric acid solution containing the nitrate radical.

A. Fundamental mode properties

In accordance with Eq. (7), at least one convex facet is required to induce stability for a ring resonator. The radius of curvature of the convex facet influences several important resonator characteristics, including beam waist size, beam ellipticity, diffractive losses, and depolarization. The optimal range for the spherical radius of curvature, R_C, is bounded by fabrication restrictions, stability requirements, and the de-

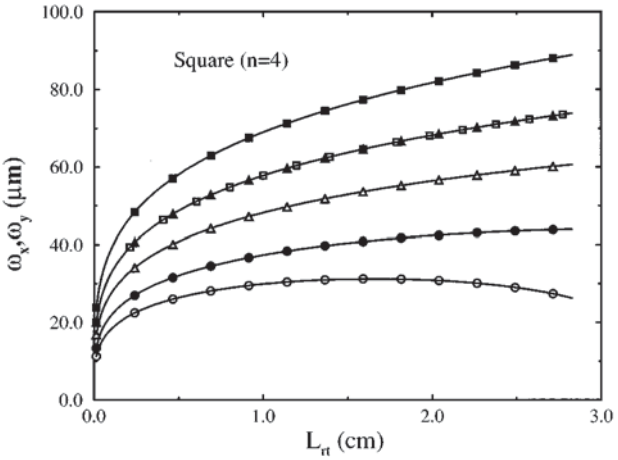

FIG. 2. The fundamental eigenmode waist sizes for astigmatic square ring resonators with a single convex facet are shown as a function of the cavity round-trip length, L_{rt}, for different radii of curvature of the convex facet. Symbol key: ω_y, $R_C=20$ (■); ω_x, $R_C=20$ (□); ω_y, $R_C=10$ (▲); ω_x, $R_C=10$ (△); ω_y, $R_C=2$ (●); ω_x, $R_C=2$ (○).

sired sampling area. The waists, ω_x and ω_y, of the astigmatic fundamental mode, which provide a lower limit for the spatial resolution of the device, are given by

$$\omega_x^2=\frac{\lambda_0 L_{rt}}{2\pi n}\left(\frac{2R_C\,\sin(\pi/n)}{L_{rt}}-1\right)^{1/2}, \tag{14}$$

$$\omega_y^2=\frac{\lambda_0 L_{rt}}{2\pi n}\left(\frac{2R_C}{L_{rt}\,\sin(\pi/n)}-1\right)^{1/2}. \tag{15}$$

Figure 2 shows the dependence of the fundamental waist size for a nominally square ($n=4$) resonator over the most useful range for L_{rt} at 633 nm for several values of the spherical radius R_C. In general, waists are located at $(1/2)L_{rt}$ from the convex facet apex, which corresponds to a flat facet for n even, and between flat facets for n odd. It is also found that $\omega_y > \omega_x$ for all values of n and R_C, and the degree of ellipticity of the fundamental mode increases with n due to the steepening angle of incidence.

Figures 3(a) and 3(b) show the stability factors (X,Y) as a function of L_{rt} for square and octagonal resonators. Each resonator, specified by n, L_{rt}, and R_C, is characterized by the pair of stability factors (X,Y) corresponding to the tangential and sagittal planes, respectively. For $R_C=2$, the stability limit $X=-1$ is reached for the octagonal resonator within this range of L_{rt}. At this limit, the waist of the lowest-order mode is no longer defined. The zero crossings for $X(R_C=2)$ indicated by the gaps in Figs. 3(a) and 3(b), correspond to the confocal condition, which has a well-defined waist but is borderline unstable. For $R_C=10$, no instability is encountered over the range of L_{rt}, while for $R_C=20$ the approach to the upper stability limit of $+1$ is apparent. The useful range of R_C narrows as n is increased, since the separation between X and Y increases. Ultimately, the lower limit on R_C is determined by fabrication constraints, the desired waist size, and the need to avoid very small waist sizes that can encourage nonspecular loss mechanisms. The upper limit is determined by the need to minimize diffraction losses for very small resonators that will have low bulk attenuation.

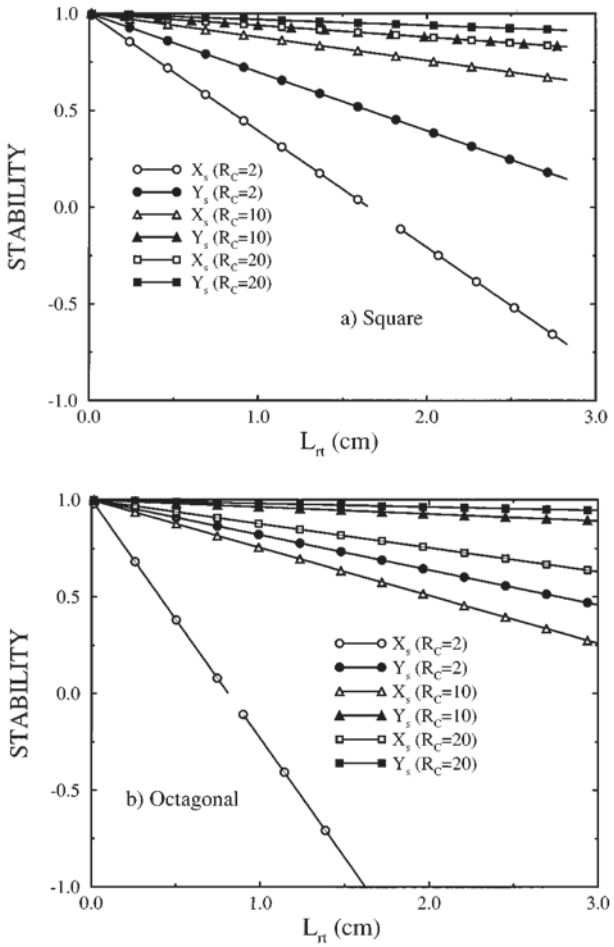

FIG. 3. Stability factors for the tangential (X_S) and sagittal (Y_S) planes for (a) square and (b) octagonal ring resonators. The gaps that are present in the stability function at the zero crossing for $X_S(R_C=2)$ correspond to the equivalent of the confocal condition for a linear resonator, which is borderline unstable.

B. Diffractive attenuation

Since the excitation of high-order transverse modes can be important in CRDS, design criteria for minimizing diffraction loss will depend on the excitation conditions. The greater attenuation of high-order modes for a given system aperture size will increase the minimum useful L_{rt}. To first establish a lower limit on resonator size for a given R_C, diffraction losses under near-perfect mode-matching conditions were examined. Figures 4(a) and 4(b) show the diffraction losses per round trip as a function of L_{rt} for square and octagonal resonators with $R_C=2$, 10, and 20 cm. The sum of bulk and surface scattering losses are also shown for relative comparison. For each value of n, L_{rt}, and R_C, the geometric mode of the resonator was found, injected into the resonator, and allowed to circulate for several passes from which an average diffractive loss was obtained. The geometric mode, which differs only slightly from the actual lowest-order eigenfunction, is the round-trip self-reproducing solution within an $ABCD$ treatment of the resonator. With near-perfect mode matching, the diffractive loss converges rapidly with the pass number, so an average over three passes provided a good estimate of the steady-state value. In Figs. 4(a) and 4(b), the diffraction loss decays with increasing L_{rt} al-

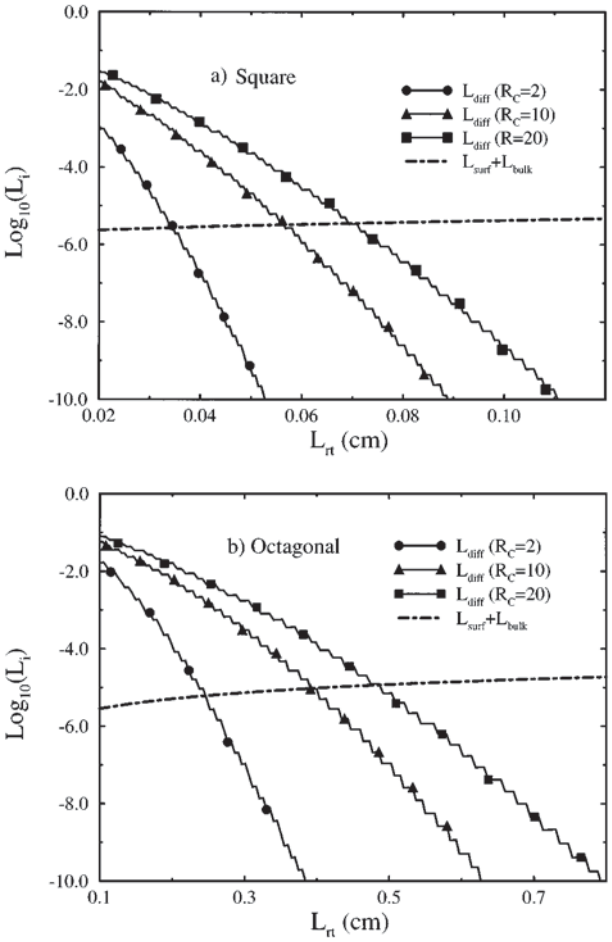

FIG. 4. The attenuation due to apertures is shown as a function of L_{rt}, under conditions of perfect mode matching, for nominally (a) square and (b) octagonal ring resonators. Three radii of curvature, $R_C = 2$, 10, and 20 cm, are considered for the single convex facet. The heavy, dot-dashed line corresponds to the sum of bulk and surface scattering losses.

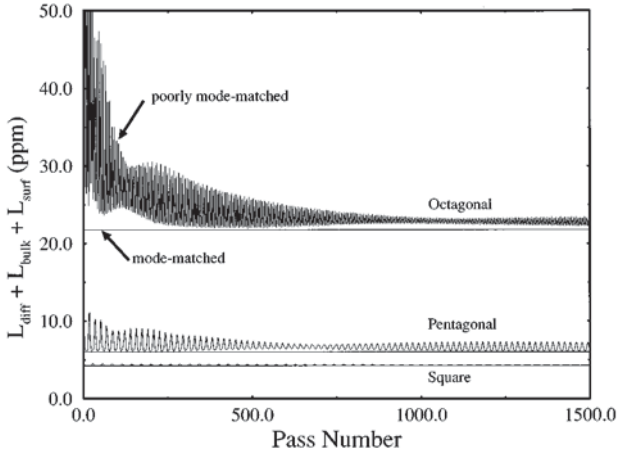

FIG. 5. The loss per pass is shown to be dependent on the number of passes (round trips) for very small cavities due to aperturing of high-order transverse modes, when mode mismatching is used. Both the mode-matched and mode-mismatched cases are shown for nominally square, pentagonal, and octagonal resonators. The perfect mode-matching case corresponds to the straight, solid lines for each geometry. The loss per pass as a function of pass number represents an alternative form of the ring-down function, which provides a time history of the loss per pass. In the case of mode mismatching, the system apertures are sufficiently small for the cavity sizes selected that a time (pass number) dependent loss per pass results as the high-order modes are selectively attenuated.

most exponentially, with more rapid fall off occurring for smaller R_C. A larger value of L_{rt} is required as n is increased to attain a given level of attenuation, due to the smaller facet size and larger angle of incidence. Figures 4(a) and 4(b) identify the lower limit for L_{rt}, since if highly efficient mode matching is achieved, a resonator with a selected n and R_C, should not have a smaller L_{rt} value than that which leads to diffraction losses of the same level as other intrinsic losses.

When mode mismatching is employed, diffraction losses become more significant. Figure 5 shows the loss per pass as a function of pass number for square, pentagonal, and octagonal resonators, which have L_{rt} values that provide an 80 dB reduction in diffractive loss or better under nearly ideal mode-matching conditions. The straight, solid lines for each resonator geometry correspond to the near-perfect mode-matching case, which yields a constant loss per pass essentially due to bulk attenuation and surface scattering. When the injected mode is poorly matched to the eigenmode of the resonator, a variable loss per pass results for these small resonators, since the apertures are sufficiently small to attenuate the higher-order modes. For each resonator, the poorly matched mode corresponds to a Gaussian beam with the same waist as the fundamental mode, but with the waist position located at the apex of the convex facet. Many modes are thereby excited, which can be characterized in terms of the coupling coefficients between the internal and excitation field distributions.[65] The calculation assumes a delta-function input pulse with a 633 nm carrier wavelength, which excites all accessible transverse modes equally for the chosen input conditions. The different Guoy shifts associated with each mode give rise to the mode beating observed in Fig. 5. The variation in the loss per pass is seen to be more severe for higher values of n, where large amplitude oscillations and low-frequency beating is apparent. The loss per pass for the octagonal resonator does approach the mode-matched value but only after many passes, which may correspond to a significant fraction of the photon decay time in some cases. In CRDS, the assumption is made that for the empty cavity all modes decay with the same time constant. Since diffraction losses are inherently transverse-mode dependent, the effects of apertures must be reduced to a negligible level for all cavity modes with significant intensity. Therefore, the design criteria for reducing diffraction losses becomes dependent on the degree of mode mismatching.

Figures 6(a) and 6(b) show diffractive losses as a function of L_{rt} for square and octagonal resonators, where the injected mode is intentionally mode mismatched. For the square geometry, the injected mode waist is located at the apex of the spherical facet with a waist size equal to three times the waist size of the fundamental mode. For the octagonal resonator, the injected mode waist is also located at the convex facet apex, but with twice the diameter of the fundamental mode, since larger values showed very large attenuation. The loss per pass for the injected mode was averaged over several passes, which yielded an upper bound for the diffractive loss, since many passes were required to

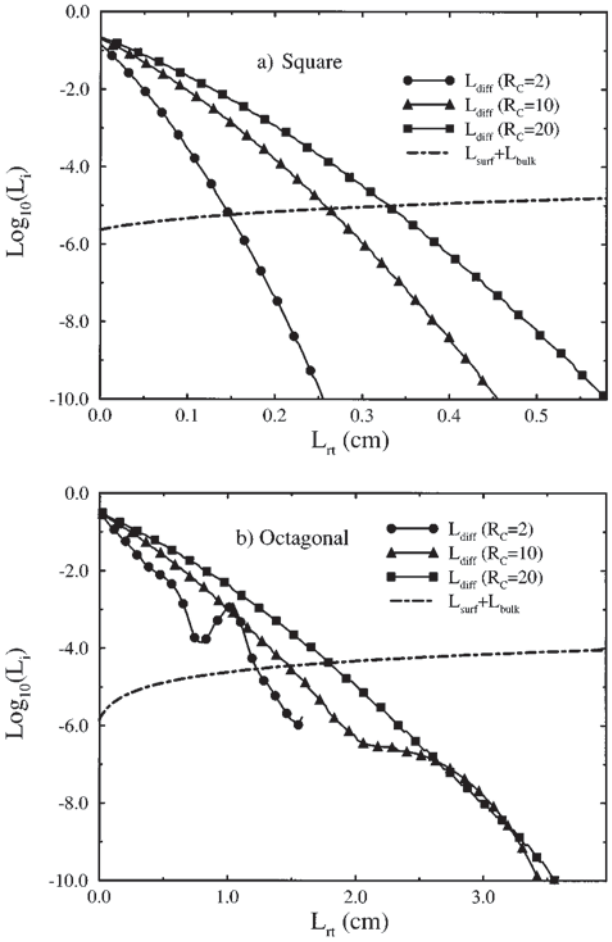

FIG. 6. The attenuation due to apertures is shown as a function of L_{rt}, when intentional mode mismatching is utilized, for nominally (a) square and (b) octagonal ring resonators. Three radii of curvature, $R_C=2$, 10, and 20 cm, are considered for the single convex facet. The heavy, dot-dashed line corresponds to the sum of bulk and surface scattering losses.

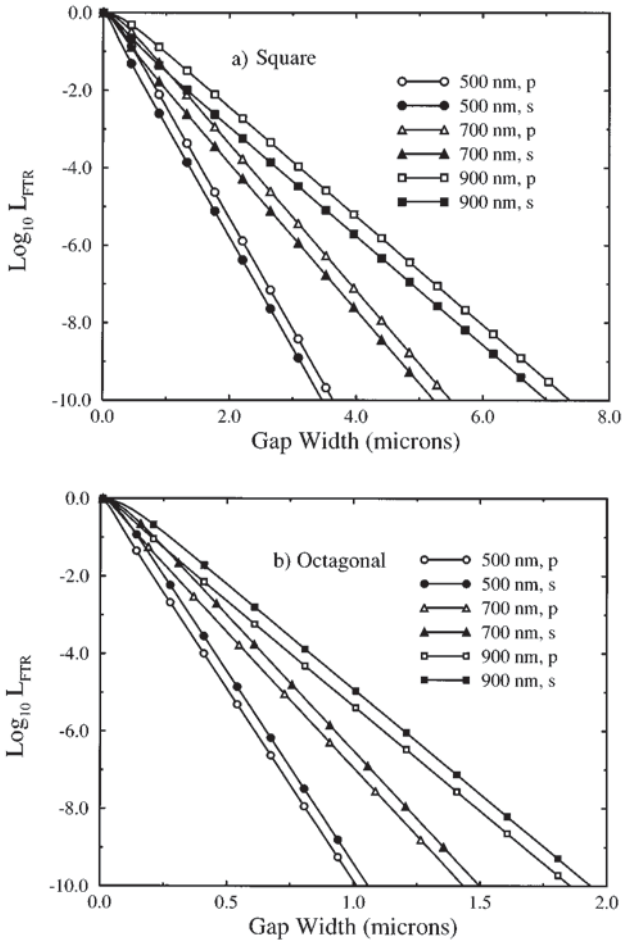

FIG. 7. Coupling efficiency for photon tunneling is shown as a function of separation between the coupling element and the resonator for nominally (a) square and (b) octagonal resonators at several wavelengths and both polarizations. The logarithmic plot emphasizes the weak-coupling regime.

achieve steady state for some values of L_{rt}. Figures 6(a) and 6(b) show greater deviation from simple exponential decay than is observed for near-perfect mode-matching conditions. For the octagonal resonator with $R_C=2$, the $X_s=0$ and $X_s=-1$ instability points are encountered, which greatly perturb diffraction losses. In general, the L_{rt} values that are required to render diffractive losses as negligible are much larger for mode-mismatched cavities. An optimum value of L_{rt} should exist for selected excitation conditions that minimizes resonator total loss through a competition between bulk attenuation and diffractive loss. If a sufficiently long photon decay time to permit accurate digitization is achieved for the optimum L_{rt}, when surface scattering and coupling losses are also included, then a miniature-cavity ring-down spectrometer becomes feasible.

C. Coupling loss

The coupling loss by photon tunneling is strongly dependent on gap width, wavelength, angle of incidence, and polarization. Figures 7(a) and 7(b) show coupling loss as a function of gap width for square and octagonal resonators, where an air-filled gap is assumed. Both *s* (out-of-plane) and *p* (in-plane) polarizations are considered for three wavelengths. The logarithmic plots of Fig. 7 emphasize the weak-coupling regime, which is characteristic of large gap widths. In general, coupling loss increases exponentially with wavelength at a fixed gap width, since the penetration depth of the evanescent field is proportional to wavelength. The polarization dependence reveals stronger coupling for *p* polarization for the square cavity and stronger *s*-polarization coupling for the octagonal cavity with an air-filled gap. As the angle of incidence moves away from the critical angle (increasing *n*), coupling loss decreases sharply for a given gap width, as manifested by the large difference in gap width required to obtain the same coupling loss for the square and octagonal resonators. The gap width required to achieve a selected coupling loss could be increased for the octagonal resonator by using a gap medium other than air. Gap widths that are 1 μm or greater are desirable to facilitate the use of interferometry for monitoring the gap width and for reducing the surface flatness requirements.

D. Polarization properties

The polarization dependence of photon tunneling, along with the polarization preserving character of monolithic, TIR-ring resonators, has been applied effectively to construct efficient harmonic conversion devices.[22,23] For spectroscopic

applications, extraction of polarization-dependent information from optical absorption measurements would greatly enhance the utility of an evanescent wave CRDS device. When a linearly polarized beam is injected into a TIR-ring resonator, polarization cross coupling can be induced by pyramidal error, surface curvature, and stress birefringence. Pyramidal error, which results when the TIR surface normals deviate from the plane of the resonator, can induce polarization cross coupling, since the phase shift that occurs at a TIR surface differs for orthogonal polarization components, thereby generating elliptical polarization. This phase shift has a maximum value of π at $\theta_i = \theta_c$ and 90°, and attains a minimum value between these limits.[66] For a pyramidal error of 0.1°, a polarization conversion of ~3 ppm is incurred. Similarly, curved surfaces induce polarization cross coupling, since the orientation of the local surface coordinate system in which the orthogonal polarization components are defined, varies as a function of position. Polarization conversion is largest for high-curvature surfaces, but for the curvatures considered here, the degree of depolarization was found to be on the order of only a few ppm. The more significant source of depolarization is stress birefringence, which induces an index variation, Δn, between orthogonal polarization states that gives rise to a retardation per round trip, Γ, given by

$$\Gamma = \frac{2\pi}{\lambda} \Delta n L_{\mathrm{rt}}. \tag{16}$$

For high-quality optical materials, an index variation of $\Delta n \sim 5 \times 10^{-7}$ is typical, which gives rise to a maximum polarization conversion of ~0.25% per cm at 633 nm. This degree of polarization cross coupling should not preclude polarization-dependent phenomena from being probed.

E. Optimum cavity design

A monolithic cavity implementation of CRDS becomes feasible only if appreciable photon decay times can be obtained to permit accurate digitization. Photon decay times on the order of microseconds, which are commonly encountered in conventional CRDS, can be accurately digitized to provide a minimum detectable relative change in the decay time of ~0.2%–1.0%.[1] To facilitate the detection of very small absorptions, the total intrinsic loss of the system must also be small. A minimum in the intrinsic loss as a function of L_{rt} should exist, which arises from the competition between bulk and diffractive losses for chosen excitation conditions. Figures 8(a) and 8(b) show the photon decay time (heavy solid line) as a function of L_{rt} for square and octagonal resonators, where the mode-mismatching conditions of Fig. 6 have been employed. The total system loss (long-dashed curves), including bulk, surface, diffractive, and coupling losses, and the sum of surface plus bulk losses (circles), are also shown, corresponding to the right-hand axis. Note that the photon decay time increases sharply as diffraction losses decrease to yield decay times that are on the order of a microsecond. As L_{rt} is increased further, the decay time approaches a constant value. The rapid rise in the decay time occurs over the range of L_{rt}, where the total system loss minimizes. The value of L_{rt} that provides the smallest total system loss will provide

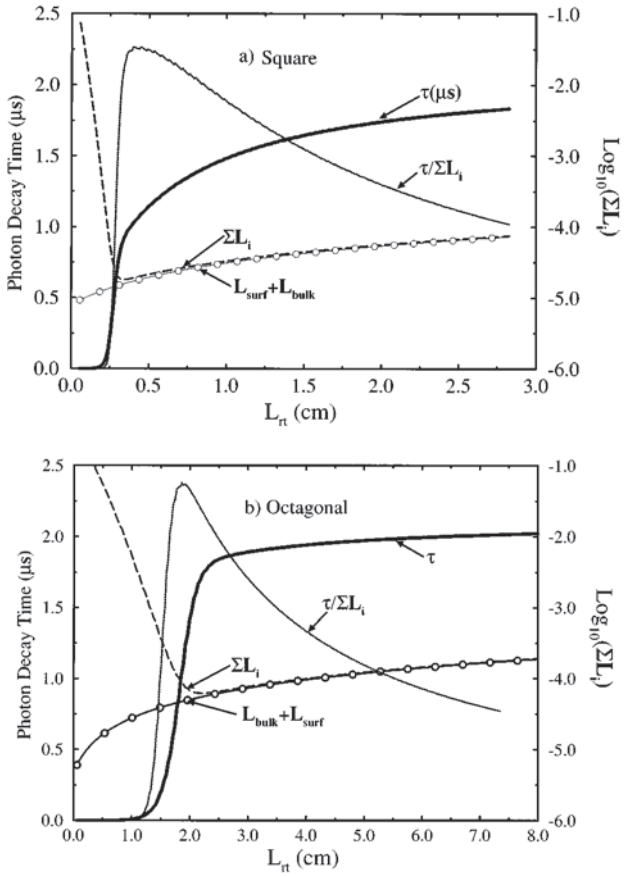

FIG. 8. An optimal cavity size is found, based on selected mode-mismatching conditions, for the (a) square and (b) octagonal resonator geometries. The heavy, solid curves describe the photon decay time as a function of L_{rt}. The long-dashed curve and line demarked by opaque circles, correspond to the right-hand-side axis and describe the total loss and the sum of bulk and surface losses, respectively. The photon decay time is seen to increase rapidly as diffraction losses decline and to asymptotically approach a constant value in the limit of large L_{rt}. The total loss function displays a minimum at which the sensitivity for detecting small absorbance changes will be maximized. The dotted line corresponds to the ratio of the round-trip time to the square of the cavity losses, which provides a measure of sensitivity. This function is plotted for relative comparison only and does not correspond to either ordinate.

the lowest detection limit. Also shown in Figs. 8(a) and 8(b) for relative comparison is the ratio of the photon decay time to the total system loss (dotted curves), which is proportional to the derivative of the photon decay time with respect to loss. This function, which provides a measure of sensitivity, shows a maximum in the vicinity of the total loss minimum. An optimum value for the cavity size, therefore, exists that minimizes the total intrinsic loss, while providing appreciable photon decay times. Calculations for the case of near-perfect mode matching, which are not shown, revealed similar functional forms to those shown in Fig. 6, but with a lower minimum loss, which occurred at smaller L_{rt}.

F. Calculated spectra

To demonstrate the performance of a TIR-ring resonator as an evanescent wave CRD spectrometer, a calculated absorption spectrum for the nitrate radical in $2\ \mathrm{mol\ L^{-1}} HNO_3$ ($n_0 = 1.35$) is presented in Fig. 9. An octagonal, ultra-high-purity-glass ($n_1 = 1.52$, -20 dB/km),

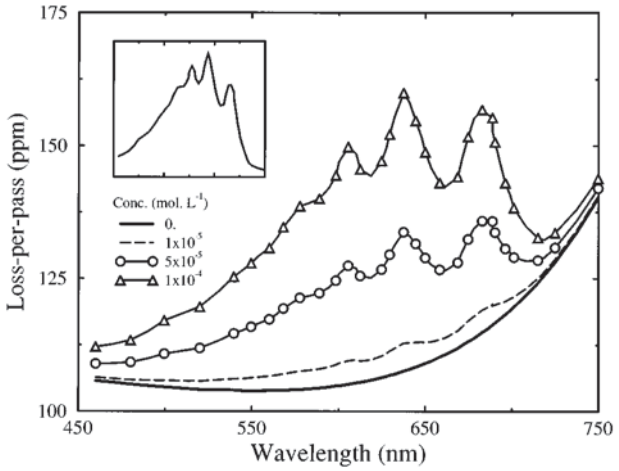

FIG. 9. Calculated spectra of the nitrate radical in 2 mol L^{-1} HNO_3 ($n = 1.35$) are shown for different radical concentrations. A high-purity-glass ($n_i = 1.52$ and -20 dB/km), TIR-ring, octagonal resonator with $L_{rt} = 2.105$ cm has been assumed to obtain the spectra. The ordinary solution-phase transmission spectrum is also shown in the inset for line-shape comparison.

resonator was assumed in the calculation, since a higher-index material than fused silica is required to prevent radiative losses when a dense, bulk solution is probed. The value for L_{rt} is 2.105 cm, which corresponds to the resonator size that minimizes the total system loss ($\Sigma \mathscr{L}_i = 1.11 \times 10^{-4}$), as discussed in Sec. IV E. The nitrate radical was selected for its relatively structured absorption spectrum in the visible region. The conventional transmission spectrum of NO_3, obtained after pulse radiolysis of 6 mol $L^{-1}HNO_3$, is also shown in the inset plot for comparison of spectral features. Absorption cross-section data for NO_3 were obtained by using the spectrum of Neta and Huie[67] and the molar extinction coefficient of Wine *et al.*[68] ($\epsilon_{635\,nm} = 830$ mol L^{-1} cm^{-1}). The evanescent wave absorption, occurring at six facets, was rigorously incorporated in the calculations by using the formulation of Hansen[69] for attenuated total reflection by a bulk solution. Some spectral distortion, due to the wavelength dependence of the effective sampling depth is apparent, although for the relative refractive index of $n_i/n_0 = 0.888$, the difference of 4.85° between the critical angle and the angle of incidence provides an absorptionlike rather than dispersionlike spectrum.[33] A detection limit of 1×10^{-6} mol L^{-1} is found, assuming a minimum detectable change in the photon decay time of 0.5%. With an effective thickness of approximately 1.2 μm at 635 nm, these results demonstrate that evanescent wave CRDS can be used to detect small concentrations of moderate absorbers in thin films.

A wave-optics model has been employed to explore the feasibility of a minicavity implementation of CRDS that utilizes the unique properties of total reflection to form a sensitive, broadband, optical absorption probe. The approach combines cavity ring down and ATR spectroscopies to extend the advantages of ATR into the trace analysis regime. An optimum cavity design is predicted to exist, which provides appreciable photon decay times and high sensitivity for the measurement of small absorbance changes. The optimum design depends on the intended application and excitation conditions. Quantitative evaluation of diffraction losses is critical for the determination of a precisely optimized design. However, the relatively slow rate of change of bulk attenuation with cavity round-trip length as shown in Fig. 8 suggests that a larger cavity than the optimal size will also provide good sensitivity. The calculations presented here are intended to provide guidance for the selection of an appropriate cavity design for a given application. Although monolithic cavities that are fabricated from conventional high-transmission optical materials have been the focus of this work, liquid cavities or cavities fabricated by molecular beam epitaxy could widen the range of application of the concept.

[1] A. O'Keefe and D. A. G. Deacon, Rev. Sci. Instrum. **59**, 2544 (1988).
[2] P. Zalicki and R. N. Zare, J. Chem. Phys. **102**, 2708 (1995).
[3] K. K. Lehmann and D. Romanini, J. Chem. Phys. **105**, 10 263 (1996).
[4] J. T. Hodges, J. P. Looney, and R. D. Van Zee, J. Chem. Phys. **105**, 10 278 (1996).
[5] R. T. Jongma, M. G. H. Boogaarts, I. Holleman, and G. Meijer, Rev. Sci. Instrum. **66**, 2821 (1995).
[6] R. Engeln and G. Meijer, Rev. Sci. Instrum. **67**, 2708 (1996).
[7] N. J. Brown, Annu. Rev. Mater. Sci. **16**, 371 (1986).
[8] E. H. Wahl, T. G. Owano, C. H. Kruger, P. Zalicki, Y. Ma, and R. N. Zare, Diam. Relat. Mater. **5**, 373 (1996).
[9] D. Romanini and K. K. Lehmann, J. Chem. Phys. **105**, 68 (1996).
[10] J. Pearson, A. J. Orr-wing, M. N. R. Ashfold, and R. N. Dixon, J. Chem. Soc. Faraday Trans. **92**, 1283 (1996).
[11] P. Zalicki, Y. Ma, R. N. Zare, E. H. Wahl, J. R. Dadamio, T. G. Owano, and C. H. Kruger, Chem. Phys. Lett. **234**, 269 (1995).
[12] J. J. Scherer, J. B. Paul, C. P. Collier, and R. J. Saykally, J. Chem. Phys. **102**, 5190 (1995).
[13] D. L. Huestis, R. A. Copeland, K. Knutsen, T. G. Slanger, R. T. Jongma, M. G. H. Boogaarts, and G. Meijer, Can. J. Phys. **72**, 1109 (1994).
[14] L. Zhu, D. Kellis, and C. F. Ding, Chem. Phys. Lett. **257**, 487 (1996).
[15] T. Yu and M. C. Lin, J. Phys. Chem. **99**, 8599 (1995).
[16] L. Zhu and G. Johnston, J. Phys. Chem. **99**, 15 114 (1995).
[17] T. Yu and M. C. Lin, Combust. Flame **100**, 169 (1995).
[18] E. W. Diau, T. Yu, M. A. G. Wagner, and M. C. Lin, J. Phys. Chem. **98**, 4043 (1994).
[19] G. Meijer (private communication). Miejer's group has examined the direct extension of CRDS to thin films by judiciously locating a thin, sapphire plate inside a linear cavity. Although a round-trip loss of $\sim 10^{-3}$ was obtained, they found that the narrow bandwidth of the cavity greatly restricted the useful range of application of this strategy.
[20] A. V. Nurmikko, H. Jeon, R. L. Gunshor, and J. Han, J. Cryst. Growth **159**, 644 (1996).
[21] S. Ando, N. Kobayashi, and H. Ando, Jpn. J. Appl. Phys. 2, Lett. **34**, 2, Lett. L4 (1995).
[22] S. Schiller and R. L. Byer, J. Opt. Soc. Am. B **10**, 1696 (1993).
[23] K. Fiedler, S. Schiller, R. Paschotta, P. Kürz, and J. Mlynek, Opt. Lett. **18**, 1786 (1993).
[24] A. Mekis, J. U. Nöckel, G. Chen, A. D. Stone, and R. K. Chang, Phys. Rev. Lett. **75**, 2682 (1995).
[25] M. D. Barnes, C-Y. Kung, W. B. Whitten, and J. M. Ramsey, Phys. Rev. Lett. **76**, 3931 (1996).
[26] M. D. Barnes, W. B. Whitten, and J. M. Ramsey, Chem. Phys. Lett. **227**, 628 (1994).
[27] J. Zhang, D. H. Leach, and R. K. Chang, Opt. Lett. **13**, 270 (1988).
[28] J. C. Knight, N. Dubreuil, V. Sandoghdar, J. Hare, V. Lefèvre-Sequin, J. M. Raimond, and S. Haroche, Opt. Lett. **12**, 698 (1996).
[29] G. Griffel, S. Arnold, D. Taskent, A. Serpengüzel, J. Connolly, and N. Morris, Opt. Lett. **21**, 695 (1996).
[30] E. Almaas and I. Brevik, J. Opt. Soc. Am. B **12**, 2429 (1995).
[31] M. L. Gorodetsky and V. S. Ilchenko, Opt. Commun. **113**, 133 (1994).
[32] J. J. Regan and D. R. Andersen, Comput. Phys. **49**, 49 (1991).
[33] N. J. Harrick, *Internal Reflection Spectroscopy* (Interscience, New York, 1967).
[34] N. J. Harrick and F. K. Du Pré, Appl. Opt. **5**, 1739 (1966).

[35] S. Schiller, I. I. Yu, M. M. Fejer, and R. L. Byer, Opt. Lett. **17**, 378 (1992).
[36] A. C. R. Pipino, J. W. Hudgens, and R. E. Huie, Chem. Phys. Lett. (in press).
[37] R. D. Maurer, Proc. IEEE **61**, 452 (1973).
[38] *Optical Properties of Highly Transparent Solids*, Waterville Valley, N.H., edited by S. S. Mitra and B. Bendow (Plenum, New York, 1975).
[39] P. Beckmann and A. Spizzichino, *The Scattering of Electromagnetic Waves from Rough Surfaces* (Pergamon, New York, 1963).
[40] H. Hogrefe and C. Funz, Appl. Opt. **26**, 2851 (1987).
[41] S. Schiller, Ph.D. thesis, Stanford University, 1993.
[42] X. Wang, G. Hu, Y. Li, and J. Yao, J. Opt. Soc. Am. A **11**, 2265 (1994).
[43] K. K. Li, Appl. Opt. **21**, 967 (1982).
[44] K. K. Li, A. Dienes, and J. R. Whinnery, Appl. Opt. **20**, 407 (1981).
[45] W. W. Rigrod, Bell Syst. Tech. J. **May**, 907 (1965).
[46] H. Kogelnik and T. Li, Proc. IEEE **54**, 1312 (1966).
[47] A. G. Fox and T. Li, Bell Syst. Tech. J. **March**, 453 (1961).
[48] A. E. Seigman, *Lasers* (University Science Books, Mills Valley, CA, 1986).
[49] J. J. Scherer, D. Voelkel, D. J. Rakestraw, J. B. Paul, C. P. Collier, R. J. Saykally, and A. O'Keefe, Chem. Phys. Lett. **245**, 273 (1995).
[50] G. Meijer, M. G. H. Boogaarts, R. T. Jongma, and D. H. Parker, Chem. Phys. Lett. **217**, 112 (1994).
[51] J. W. Strutt, Philos. Mag. **5.6 20**, 1001 (1910).
[52] G. Meijer and R. Engeln, Chem. Phys. Lett. **262**, 105 (1996).
[53] D. Romanini, A. A. Kacchanov, and F. Stoeckel, Chem. Phys. Lett. **264**, 316 (1997).
[54] B. A. Paldus, J. S. Harris, J. Martin, J. Xie, and R. N. Zare, J. Appl. Phys. (in press).
[55] G. Rempe, R. J. Thompson, H. J. Kimble, and R. Lalezari, Opt. Lett. **17**, 363 (1992).
[56] J. W. Goodman, *Introduction to Fourier Optics* (McGraw-Hill, New York, 1968).
[57] A. K. Ghatak and K. Thyagarajan, *Contemporary Optics* (Plenum, New York, 1978), p. 331.
[58] A. K. Ghatak, M. R. Shenoy, I. C. Goyal, and K. Thyagarajan, Opt. Commun. **56**, 313 (1986).
[59] F. Falco and T. Tamir, J. Opt. Soc. Am. A **7**, 185 (1990).
[60] W. Nasalski, J. Opt. Soc. Am. A **13**, 172 (1995).
[61] K. Ohta and H. Ishida, Appl. Opt. **29**, 1952 (1990).
[62] I. N. Court and F. K. Von Willisem, Appl. Opt. **3**, 719 (1964).
[63] G. Lawrence, *Applied Optics and Optical Engineering* (Academic, New York, 1992), Vol. 11, p. 168. The GLAD code required modification to permit photon tunneling, evanescent wave absorption, and utilization of a global coordinate system for the general polygonal ring resonator model. Note that identification of specific commercial products in this paper is provided in order to specify procedures completely. In no case does such identification imply recommendation or endorsement by the National Institute of Standards and Technology, nor does it imply that such products have necessarily been identified as the best available for the purpose.
[64] F. D. Feiock, J. Opt. Soc. Am. **68**, 485 (1978).
[65] F. Bayer-Helms, Appl. Opt. **23**, 1369 (1984).
[66] D. Clarke and J. F. Grainger, *Polarized Light and Optical Measurement* (Pergamon, New York, 1971), p. 57.
[67] P. Neta and R. E. Huie, J. Phys. Chem. **90**, 4644 (1986).
[68] P. H. Wine, R. L. Mauldin III, and R. P. Thorn, J. Phys. Chem. **92**, 1156 (1988).
[69] W. N. Hansen, Spectrochim. Acta **21**, 815 (1965).